

## Determination of welding heat source parameters for fem simulation based on temperature history and real bead shape

SZYNDLER Joanna<sup>1,a \*</sup>, SCHMIDT Alexander<sup>1,b</sup> and HÄRTEL Sebastian<sup>1,c</sup>

<sup>1</sup>Chair of Hybrid Manufacturing, Brandenburg University of Technology, Cottbus, Germany

<sup>a</sup> Joanna.Szyndler@b-tu.de, <sup>b</sup> Alexander.Schmidt@b-tu.de, <sup>c</sup> Sebastian.Haertel@b-tu.de

**Keywords:** Finite Element Method (FEM), Wire Arc Additive Manufacturing (WAAM), Calibration Procedure, Goldak's Heat Source Parameters

**Abstract.** To improve process understanding and increase the numerical prediction quality of a wire arc additive manufacturing (WAAM) process, this paper focuses on determining the parameters of a numerical model that reproduces an experimental setup of a welding process, with particular attention given to the actual shape of the weld bead. The dimensions of the heat source (HS) model in a welding process are determined based on experimentally measured weld pool sizes as well as temperature history at selected points below and adjacent to a weld seam. The whole experimental setup is accurately reproduced within the Simufact.Welding software and an optimization procedure is applied to obtain the best possible agreement between experimental and numerical results. A validated numerical model with reliable parameters for two heat sources is later used to predict and observe material behavior during the WAAM process of more complex parts.

### Introduction

The wire arc additive manufacturing process is becoming increasingly popular in many engineering industries due to its high deposition rate, low costs, nearly unlimited build size, and near-net shape manufacturing of complex geometries. It enables the production of structurally efficient and free-formed shapes in a shorter time as compared to other AM processes. Moreover, varied materials can be applied together to obtain functionally graded materials [1,2]. The main advantage of WAAM is its ability to manufacture high-quality parts with strong structural and mechanical properties. All these and other advantages of the WAAM process are the reason for many research works focused on its applicability in aerospace, automotive, biomedical, or marine industries [3-7]. Most of the focus is concentrated on the microstructure and mechanical properties of the manufactured parts [8], controlling deposition shape [9], and analysis of the residual stress or distortions [10,11].

WAAM is executed by depositing subsequent layers of molten metal on top of each other until the expected geometry is created. Welding metals is a process that includes heating and cooling cycles, which strongly influences chemical-metallurgical reactions in liquid metal, phase transformations, grain growth, and therefore final material mechanical properties [12]. To better understand the mechanisms taking place during WAAM and to minimize the costs of experimental investigations at the same time, a simulation approach is eagerly applied, where not only finite element models [11,13-17], but also neural networks [16,18,19] or mathematical [20], recursive models [21] are increasingly used. However, to accurately simulate the final properties of the part obtained by the WAAM process, a realistic heat source shape and distribution is necessary [22].

Thus, to improve the understanding of the material behavior during a WAAM process, this work aims to determine the parameters of a numerical model that reproduces the welding process, with particular attention given to the actual shape of the weld bead. In this study, the dimensions of Goldak's heat source [23] model in a welding process are determined based on experimentally



measured weld pool sizes as well as temperature history at selected points below and adjacent to a weld seam.

### Experimental Procedure

The welding experiments have been conducted with an Arc 605 WAAM system of GEFERTEC GmbH (Berlin, Germany). As welding material, AWS A5.18 with a wire diameter of  $\varnothing = 1.2$  mm was chosen. The chemical composition of the welding material is stated in Table 1. To conduct the temperature measurement a DMC Plus measuring amplifier of HBM (Darmstadt, Germany) was used.

*Table 1. Chemical composition of AWS A5.18 % weight.*

C	Mn	Si	Cu	Fe
0.06 - 0.13	1.4 - 1.6	0.7 - 1.0	$\leq 0.3$	Rest

To ensure the reproducibility of the experiments and reproduce a real WAAM process concerning the thermal characteristics as far as possible a device was constructed as shown in Fig. 1a. All the parts are made of AISI 1045, which is considered to be sufficiently comparable to the AWS A5.18 and thus a real WAAM component of AWS A5.18 concerning the thermal characteristics. Since the measurement of the melt pool temperature is not possible during the welding, the temperature measurement took place at four relevant points near the welding seam via type K thermocouples. To improve the response time of the thermocouples, the thermocouples were spot-welded at the indicated positions. In detail, the temperature was measured at the upper substrate surface near the welding seam (TC 1), at the lower substrate surface directly below the welding seam (TC 2), and at two points within the base plate at different distances to the welding surface (TC 4 and TC 5), as seen in Fig. 1b.

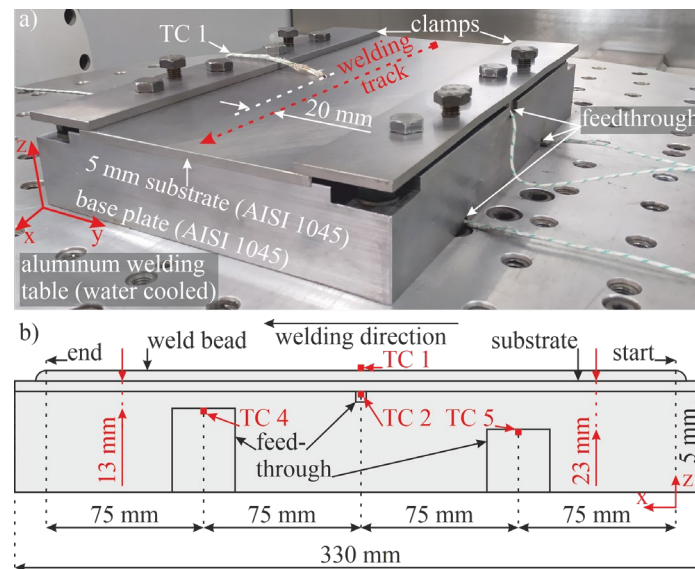


*Fig. 1. Experimental setup for welding experiments with temperature measurement a) macroscopic image and b) cross-sectional sketch indicating positions of the thermocouples.*

Since the melt pool characteristic is not stable when starting the welding process and thus not representative for the weld bead, the temperature measurement took place at least 75 mm after the starting of the welding process to ensure a quasi-static process state (Fig. 1b). With the device it is possible to perform welding experiments with and without preheating the substrate. The preheating of the substrate and the device enables the reproduction of the welding process of a real component in higher detail. In this case, preheating was not applied and thus the starting temperature of the

substrate was room temperature. Other relevant welding parameters are shown in Table 2. Subsequent scanning electron microscope (SEM) analyses of the welding seam were conducted with a Phenom XL G2 of ThermoFisher Scientific (Waltham, USA).

Table 2. Welding process parameter.

Welding mode [-]	CMT-process frequency [Hz]	Process gas [-]	Gas flow rate [l/min]	Current [A]	Voltage [V]	Feedstock velocity [mm/min]	Axis speed [mm/min]
Cold metal transfer (CMT)	3	Ar18CO <sub>2</sub>	15	144	14.6	4,000	400

## Results and Discussion

Temperature history plots show the highest recorded value (712°C) directly under the weld seam at the location of TC 2. The second highest temperature is noted by TC 1 – 180°C – on the top surface of the substrate. Thermocouples 4 and 5 record ca. 100 and 50°C as maximum values of observed temperatures (Fig. 2). Although TC 1 and TC 2 are in the same cross-section, the peaks of the respective temperature plots are temporally shifted to each other. TC 2 temperature plot represents the heat transfer from the electric arc, which is a moving HS, into the material by conduction. TC 2 temperature rises within a few seconds when the electric arc is passing the cross section above TC 2 and is falling shortly after the electric arc passed the relevant cross-section. TC 1 temperature history represents the heat transfer from the welding seam to TC 1 through the substrate by heat conduction. Thus, as long as the welding seam (TC 2) has a significantly higher temperature it acts as a stationary heat source regarding TC 1. Since TC 1 is 20 mm away from the welding seam and heat transfer by conduction takes time, the peak of TC 1 is delayed compared to TC 2.

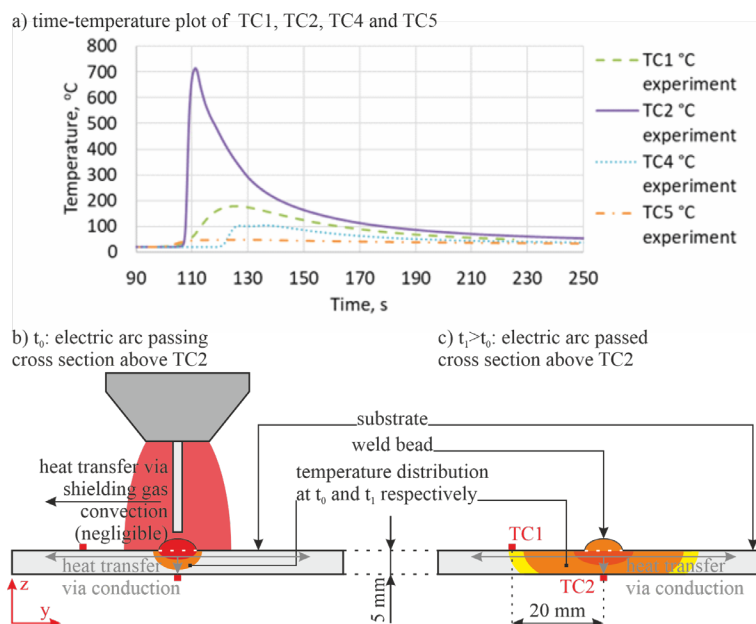


Fig. 2. a) Temperature history recorded by four thermocouples during the welding process of a single weld seam, b) schematic sketch of welding process at  $t_0$  and c) schematic sketch of welding process at  $t_1 > t_0$ .

As is presented in Fig. 3a, SEM analyses are made in two locations: first at the cross-section in the middle of the weld seam (V1); second at the cross-section in the longitudinal direction at the end of the weld seam (V2). Fig. 2b shows that the depth of the fully melted zone of the base material

reaches  $\sim 1.41$  mm during the welding process. A mixture of liquid and austenite phases existed till the  $\sim 1.9$  mm level during the welding process. Lastly, the heat-affected zone reached a depth of  $\sim 3.5$  mm. The longitudinal cross-section V2 enabled the estimation of the amount of material that overflows in the front and rear direction (Fig. 3c), which enabled the prediction of the initial values of the front and rear lengths of Goldak's heat source model. It is also visible there that the depth of the melted zone is not constant in a vertical direction and varies along the weld seam, which might be a result of the cold metal transfer mode.

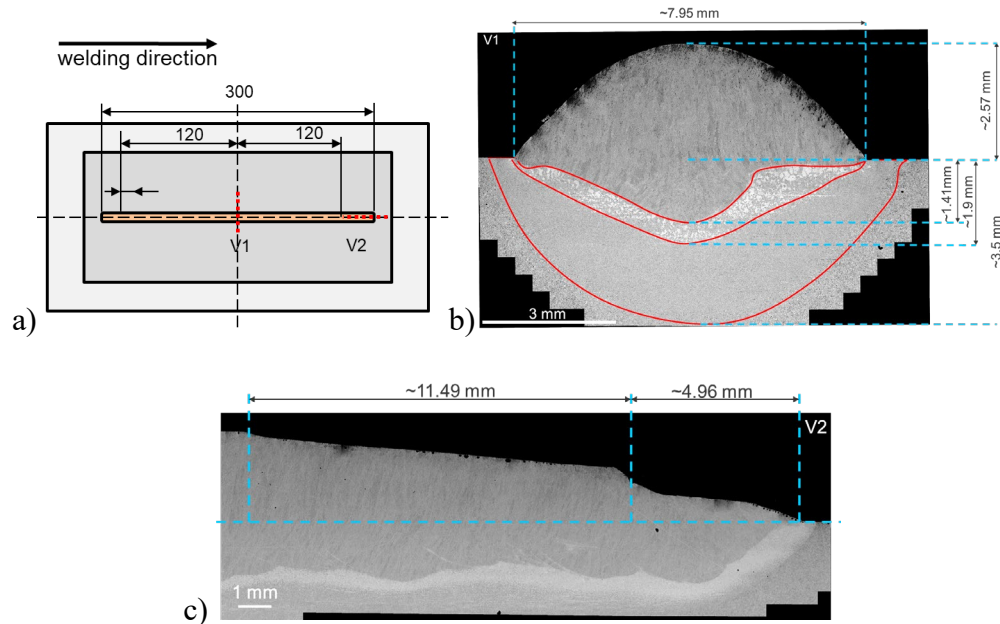


Fig. 3. a) Locations of the SEM analyses; b) in the middle of the seam, c) at the end of the seam in the longitudinal direction.

### Numerical Simulation

To reproduce the experimental setup in a digital form, the Simufact.Welding 2021.1 software (Hexagon, Stockholm) is used, where a ground plate, substrate plate, and holding clamps are also included in the FE model (Fig 4a). To minimize the influence of the geometry of the weld seam on the quality of obtained results, a cross-section from metallography (Fig. 3b) was applied to represent the expected shape of the welding seam (Fig 4b).

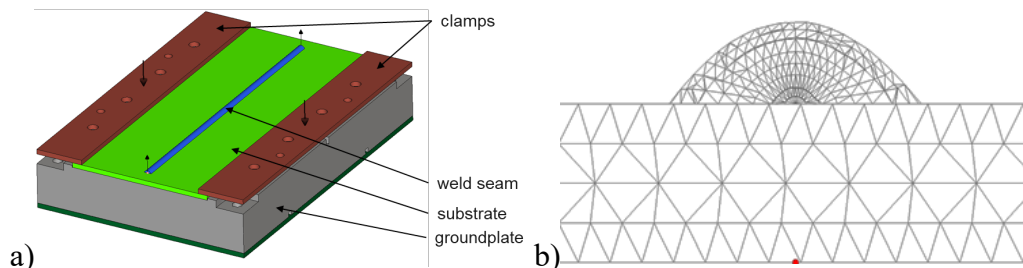


Fig. 4. FE model developed in Simufact. Welding software: a) full setup, b) cross-section of the weld seam.

Material properties of the AISI 1045 steel substrate, such as density and thermal capacity are taken from the literature [24, 25] (Fig. 5a, b), whereas thermal conductivity was measured with Linseis LFA 1000 Laser Flash test machine (Linseis Messgeräte GmbH, Selb, Germany) (Fig. 5c). Material properties of the AWS A5.18 wire are taken from the Simufact.Welding 2021.1 material database.

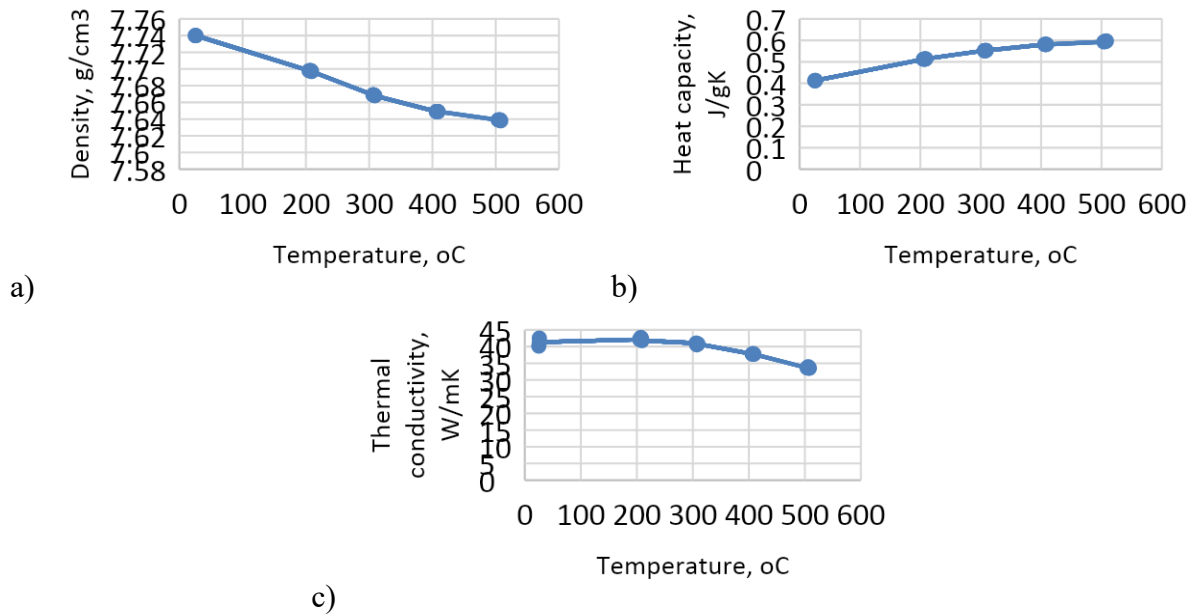


Fig. 5. Material properties of AISI 1045 as a function of temperature: a) density [24], b) heat capacity [25], c) thermal conductivity measured by Authors.

The convective heat transfer parameter  $h_{plate}$  in the function of temperature for a substrate (Fig. 6b), is calculated based on classical heat transfer equations characteristic for natural convection that is present over a flat surface facing up:

$$\beta = \frac{1}{T_f} \quad (1)$$

$$T_f = \frac{(T_s + T_\infty)}{2} \quad (2)$$

$$L_c = A_s/p \quad (3)$$

$$Ra_L = \frac{g\beta(T_s - T_\infty)L_c^3}{\nu^2} Pr \quad (4)$$

$$Nu = 0.54Ra_L^{\frac{1}{4}} \quad (5)$$

$$h_{plate} = \frac{k}{L_c} Nu \quad (6)$$

where:  $A_s$  is the top surface area of the plate,  $p$  – circumference of the plate,  $Pr$  – Prandtl number (at  $T_f$ ),  $Nu$  – Nusselt number,  $Ra_L$  – Rayleigh number,  $\nu$  – kinematic viscosity (at  $T_f$ ),  $L_c$  – characteristic length,  $T_f$  – film temperature,  $k$  – thermal conductivity (at  $T_f$ ).

The weld seam is treated as a horizontally placed cylinder, for which the natural convection parameter  $h_{cylinder}$  is presented in Fig. 6a and calculated with the following equations:

$$Nu = \left\{ 0.6 + \frac{0.387Ra_D^{\frac{1}{4}}}{\left[ 1 + \left( \frac{0.559}{Pr} \right)^{\frac{9}{16}} \right]^{\frac{8}{27}}} \right\}^2 \quad (7)$$

$$h_{cylinder} = \frac{k}{D} Nu \quad (8)$$

Properties of air at atmospheric pressure such as: kinematic viscosity  $\nu$ , thermal conductivity  $k$  and Prandtl number  $Pr$  are described as functions of temperature with following equations:

$$v = -0.0000000000000108002806777848 \text{ T}^3 + 0.0000000000784312587177112 \text{ T}^2 + 0.0000000931723588917573 \text{ T} + 0.0000131184421229409 \quad (9)$$

$$k = 0.00000000000464104563529673 \text{ T}^3 - 0.0000000252204641238776 \text{ T}^2 + 0.0000756242633211078 \text{ T} + 0.0236352337830901 \quad (10)$$

$$\begin{aligned} \text{Pr} = & 0.0000000000000000000025041212039251900 \text{ T}^6 - 0.0000000000000000207919919188157 \text{ T}^5 + \\ & + 0.000000000000067316897714983 \text{ T}^4 - 0.00000000109717750688835 \text{ T}^3 + \\ & + 0.000000941818163402441 \text{ T}^2 - 0.000346614970760939 \text{ T} + 0.737371365505794 \end{aligned} \quad (11)$$

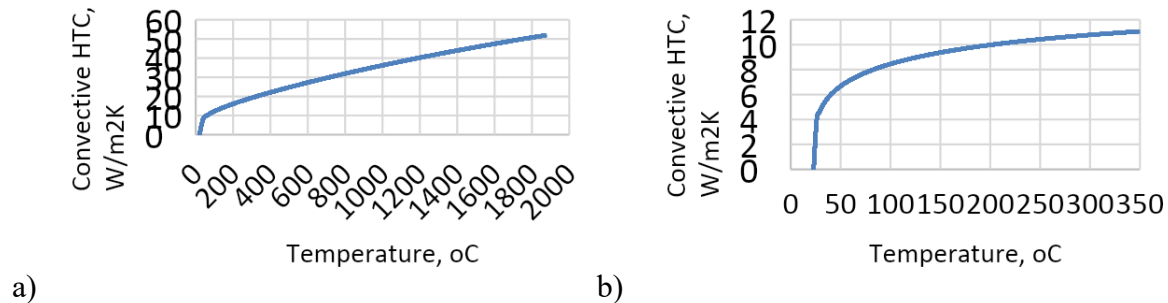


Fig. 6. Convective heat transfer coefficient as a function of the temperature of the a) weld seam, and b) substrate to air.

A single seam is welded digitally with the same speed (6.66667 mm/s), voltage (14.6 V), and current (144 A) as welding parameters applied during the real experiment. The air temperature and initial temperature of the wire are set to 23°C, the initial temperature of all plates is set to 21.5°C, and arc efficiency is assumed to be 80%.

Goldak's heat source model [23] was used to describe the volumetric heat flux density distribution, where  $a_f$ ,  $a_r$ ,  $b$ ,  $d$  are parameters related to the shape characteristic of the welding arc (Fig. 7). Values of the front (4.96 mm) and rear (11.49 mm) length of the heat source one, are read from the microscopic analysis presented in Fig. 3c. Values of the width and depth parameters are established based on optimization procedure applied to obtain a similar picture of the melted zone between the simulation and experiment. During this procedure, an advantage of applying two heat sources was used [26], which enabled to improve results in terms of temperature history recorded during the real test, especially on the top surface of the substrate. A targeted adjustment of the parameters for both HSs was done at the same time, to compare the calculated shape of the fusion zone and temperature history to the experimental data shown in Fig. 2 and 3b. The final values of the obtained parameters of both heat sources are gathered in Table 3.

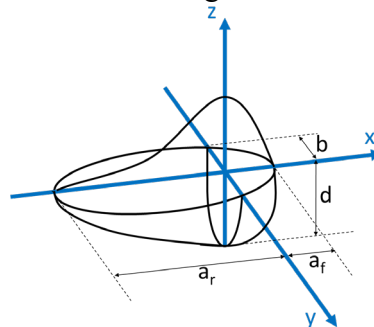


Fig. 7. Goldak's double ellipsoid heat source model;  $a_f$  – front length,  $a_r$  – rear length,  $b$  – width,  $d$  – depth.



*Table 3. Obtained Goldak's heat source parameters.*

	$a_f$ [mm]	$a_r$ [mm]	$b$ [mm]	$d$ [mm]
HS 1	4.96	11.49	3	2
HS 2	0.1	0.1	0.3	0.3

### Validation of the Numerical Simulation Results

The simulation results with 2 heat sources show a particularly good agreement with the available experimental data. The geometry and size of the melted zone visible directly below the weld seam agree well with the microscopic results (Fig. 8). Based on the phase diagram characteristic of AISI 1045 steel, the fully liquid phase is assumed to occur above 1525°C, a mixture of liquid and austenitic phases is observed at temperatures of 1425-1525°C, and only the austenitic phase is present at 770-1425°C. These temperature ranges are used to determine the calculated geometry of the melt zone during FE simulation. As shown in Fig. 8, the fully liquid phase can be seen to a depth of ~1.46 mm, austenite + liquid to ~1.7 mm, and the pure austenite phase to ~4 mm. In contrast, if only one heat source is used, neither the geometry nor the size of the melt zone visible directly below the weld seam is realistically calculated, as a comparison of Fig. 8b with Fig. 8c shows. Moreover, the calculated Root Mean Square Error (RMSE) (see Fig. 9) between measured and simulated temperature history (for using HS1 and HS2 together) at selected points equals 6.25, 44.6, 7.07, and 3.91°C at TC 1, TC 2, TC 4, and TC 5, respectively. Such well prepared and validated the numerical model with dependable Goldak's heat source parameters can be later used to predict and observe material behavior during the WAAM process of much more complex parts.

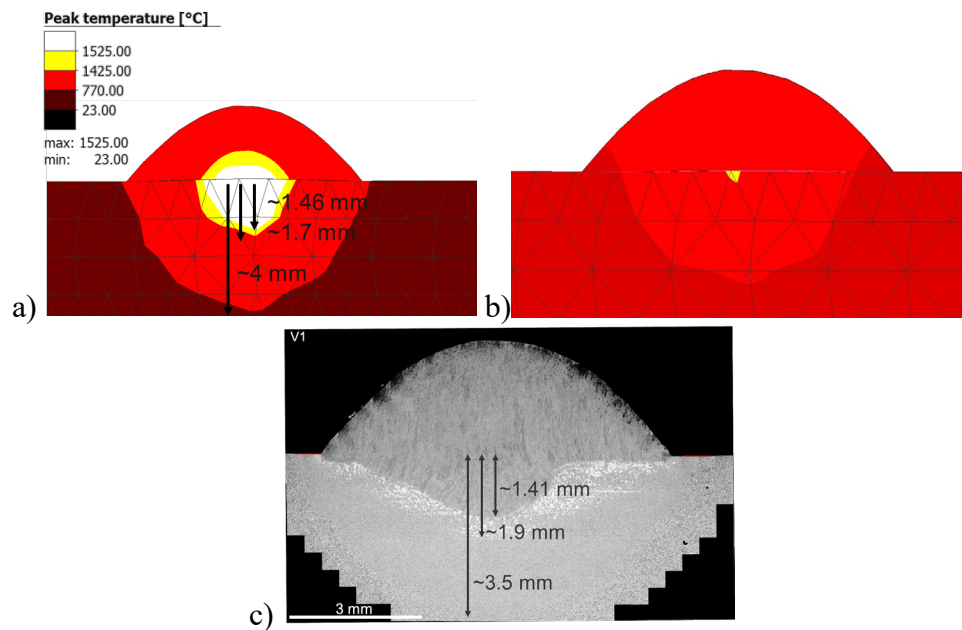


*Fig. 8. Peak temperature distribution in the middle of the weld seam according to the simulation with a) 2 HSs; b) 1 HS; b)c) SEM-image of the weld seam indicating the temperature distribution during the welding process.*

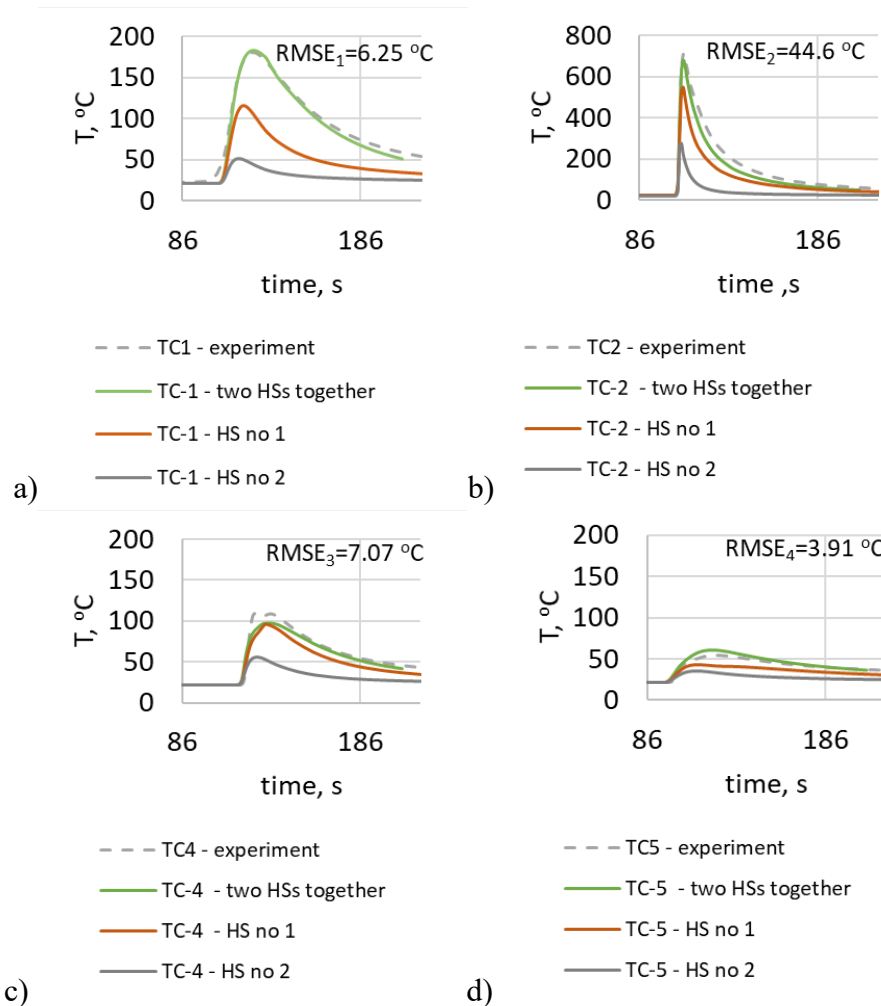


Fig. 9. Comparison between experimental (dotted lines) and numerical results (continuous lines) in terms of recorded temperature history in selected points: a) TC1, b) TC2, c) TC4, d) TC5.

For investigation purposes, also single HS models were calculated when only 1 Goldak's heat source was applied to weld a seam. Obtained results in form of temperature-time plots are presented in Fig. 9. As is noticeable, the application of the 2 HS model enables to obtain reliable temperature history at different locations of the base plate. Especially the prediction of temperature history on the top surface of the substrate is improved in comparison to the single HS model.

### Summary

In this investigation, the parameters of Goldak's heat source model are determined based on experimentally measured weld pool sizes as well as temperature history at selected points below and adjacent to a weld seam. A single 300 mm long seam of AWS A5.18 wire is welded onto an AISI 1045 base plate. Four thermocouples are measuring temperature history: first on the top surface next to the weld seam, second directly under the weld seam, and two more thermocouples are placed under the base plate on two diverse levels. A microscopic analysis of the weld seam cut in the middle of its length gives information about the expected heat zone size and is also a hint for dimensions of the Goldak's HS. The whole experimental setup is accurately reproduced within the Simufact.Welding 2021.1 software and an optimization procedure is applied to obtain the best possible agreement between experimental and numerical results. In this case, a two-heat source model gives the most accurate results, where not only a melted zone of the material is accurately



predicted but also temperature history under the substrate, under the weld seam, and on the top surface of the substrate are very close to reality.

### Acknowledgments

The IGF-project 21219 BG of the European Research Association for Sheet Metal Working (EFB e.V.) is funded by the German Federation of Industrial Research Associations (AiF) within the framework of the Industrial Collective Research (IGF) program by the Federal Ministry of Economic Affairs and Climate Action based on a decision by the German Bundestag.

The Authors would like to thank the EFB and the members of the industrial consortium for supporting the research activities.

### References

- [1] S.I. Evans, J. Wang, J. Qin, Y. He, P. Shepherd, J. Ding, A review of WAAM for steel construction – Manufacturing, material and geometric properties, design, and future directions, *Structures* 44 (2022) 1506-1522. <https://doi.org/10.1016/j.istruc.2022.08.084>
- [2] S. Singh, S.K. Sharma, D.W. Rathod, A review on process planning strategies and challenges of WAAM, *Materials Today: Proceedings*, 47, 19 (2021) 6564-6575.
- [3] V. Madhavadas, D. Srivastava, U. Chadha, S.A. Raj, M.T.H. Sultan, F.S. Shahar, A.U.M. Shah, A review on metal additive manufacturing for intricately shaped aerospace components, *CIRP J. Manuf. Sci. Technol.* 39 (2022) 18-36. <https://doi.org/10.1016/j.cirpj.2022.07.005>
- [4] J. Ye, P. Kyvelou, F. Gilardi, H. Lu, M. Gilbert, L. Gardner, An end-to-end framework for the additive manufacture of optimized tubular structures, *IEEE Access*, 9 (2021) 165476-165489. <https://doi.org/10.1109/ACCESS.2021.3132797>
- [5] X. Zuo, W. Zhang, Y. Chen, J.P. Oliveira, Z. Zeng, Y. Li, Z. Luo, S. Ao, Wire-based directed energy deposition of NiTiTa shape memory alloys: Microstructure, phase transformation, electrochemistry, X-ray visibility and mechanical properties, *Additive Manuf.* 59 (2022) 103115. <https://doi.org/10.1016/j.addma.2022.103115>
- [6] M. Vishnukumar, R. Pramod, A.R. Kannan, Wire arc additive manufacturing for repairing aluminium structures in marine applications, *Mater. Lett.* 299 (2021) 130112. <https://doi.org/10.1016/j.matlet.2021.130112>
- [7] T. Feucht, J. Lange, B. Waldschmitt, A.K. Schudlich, M. Klein, M. Oechsner, Welding process for the additive manufacturing of cantilevered components with the WAAM, *Adv. Join. Process.* 125 (2020) 67-78.
- [8] F. Wang, S. Williams, P. Colegrove, A.A. Antonysamy, Microstructure and mechanical properties of wire and arc additive manufactured Ti-6Al-4V, *Metall. Mater. Trans. A* 44 (2013) 968-977. <https://doi.org/10.1007/s11661-012-1444-6>
- [9] J. Xiong, G. Zhang, Forming appearance analysis in multi-layer single pass GMAW-based additive manufacturing, *Int. J. Adv. Manuf. Technol.* 80 (2015) 1767-1766. <https://doi.org/10.1007/s00170-015-7112-4>
- [10] P.J. Ding, J. Mehnert, S. Ganguly, P.M.A. Sequeira, F. Wang, S. Williams, Thermo-mechanical analysis of wire and arc additive manufacturing process on large multi-layer parts, *Comput. Mater. Sci.* 50 (2011) 3315-3322. <https://doi.org/10.1016/j.commatsci.2011.06.023>
- [11] X. Zhou, H. Zhang, G. Wang, X. Bai, Three-dimensional numerical simulation of arc and metal transport in arc welding based additive manufacturing, *Int. J. Heat Mass Transfer* 103 (2016) 521-537. <https://doi.org/10.1016/j.ijheatmasstransfer.2016.06.084>
- [12] A.S. Azar, S.K. As, O.M. Akselsen, Determination of welding heat source parameters from actual bead shape, *Comput. Mater. Sci.* 54 (2012) 176-182. <https://doi.org/10.1016/j.commatsci.2011.10.025>

- [13] Z. Hu, X. Qin, T. Shao, Welding thermal simulation and metallurgical characteristics analysis in WAAM for 5CrNiMo hot forging die remanufacturing, *Procedia Eng.* 207 (2017) 2203-2208. <https://doi.org/10.1016/j.proeng.2017.10.982>
- [14] C.T.J. Panicker, K.R. Surya, V. Senthilkumar, Novel process parameter-based approach for reducing residual stresses in WAAM, *Materials Today: Proceedings* 59 (2022) 1119-1126. <https://doi.org/10.1016/j.matpr.2022.03.025>
- [15] N.P. Gokhale, P. Kala, Thermal analysis of TIG-WAAM based metal deposition process using finite element method, *Materials Today: Proceedings* 44 (2021) 453-459.
- [16] Y. Ling, J. Ni, J. Antonissen, H.B. Hamouda, J.V. Voorde, M.A. Wahab, Numerical prediction of microstructure and hardness for low carbon steel wire Arc additive manufacturing components, *Simul. Model. Pract. Th.* 122 (2023) 102664. <https://doi.org/10.1016/j.simpat.2022.102664>
- [17] V. Gorniyakov, Y. Sun, J. Ding, S. Williams, Modelling and optimizing hybrid process of wire arc additive manufacturing and high-pressure rolling, *Mater. Design* 223 (2022) 111121. <https://doi.org/10.1016/j.matdes.2022.111121>
- [18] S. Bose, A. Biswas, Y. Tiwari, M. Mukherjee, S.S. Roy, Artificial neural Network-based approaches for Bi-directional modelling of robotic wire arc additive manufacturing, *Materials Today: Proceedings* 62 (2022) 6507-6513. <https://doi.org/10.1016/j.matpr.2022.04.331>
- [19] Y. Wang, X. Xu, Z. Zhao, W. Deng, J. Han, L. Bai, X. Liang, J. Yao, Coordinated monitoring and control method of deposited layer width and reinforcement in WAAM process, *J. Manuf. Process.* 71 (2021) 306-316. <https://doi.org/10.1016/j.jmapro.2021.09.033>
- [20] W.C. Ke, J.P. Oliveira, B.Q. Cong, S.S. Ao, Z.W. Qi, B. Peng, Z. Zeng, Multi-layer deposition mechanism in ultra high-frequency pulsed wire arc additive manufacturing (WAAM) of NiTi shape memory alloys, *Additive Manuf.* 50 (2022) 102513. <https://doi.org/10.1016/j.addma.2021.102513>
- [21] C. Chen, H. He, J. Zhou, G. Lian, X. Huang, M. Feng, A profile transformation based recursive multi-bead overlapping model for robotic wire and arc additive manufacturing (WAAM), *J. Manuf. Process.* 84 (2022) 886-901. <https://doi.org/10.1016/j.jmapro.2022.10.042>
- [22] J.A. Goldak, M. Akhlaghi, *Computational Welding Mechanics*, Springer, US, 2005.
- [23] J. Goldak, A.P. Chakravarti, M. Bibby, A new finite element model for welding heat sources, *Metall. Trans. B* 15 (1984) 299-305. <https://doi.org/10.1007/BF02667333>
- [24] M. Hojny, M. Glowacki, Numerical Modelling of Steel Deformation at Extra-High Temperatures, in P. Miidla (ed.), *Numerical Modelling*, IntechOpen, London, 2012. <https://doi.org/10.5772/36562>.
- [25] A. Martinovs, S. Polukoshko, E. Zaicevs, R. Revalds, Laser Hardening Process Optimizations Using FEM, *Engineering for Rural Development*, 2020, pp. 1500-1508. <https://doi.org/10.22616/ERDev2020.19.TF372>
- [26] H.M. Aarbogh, M. Hamide, H.G. Fjaer, A. Mo, M. Bellet, Experimental validation of finite element codes for welding deformations, *J. Mater. Process. Technol.* 210 (2010) 1681-1689. <https://doi.org/10.1016/j.jmatprotec.2010.05.014>